COCOON: ROBUST MULTI-MODAL PERCEPTION WITH UNCERTAINTY-AWARE SENSOR FUSION

Minkyoung Cho[1], **Yulong Cao**[2], **Jiachen Sun**[1], **Qingzhao Zhang**[1],
Marco Pavone[2,3], **Jeong Joon Park**[1], **Heng Yang**[2,4], **and Z. Morley Mao**[1]

[1]University of Michigan
[2]NVIDIA Research
[3]Stanford University
[4]Harvard University
https://minkyoungcho.github.io/cocoon/

ABSTRACT

An important paradigm in 3D object detection is the use of multiple modalities to enhance accuracy in both normal and challenging conditions, particularly for long-tail scenarios. To address this, recent studies have explored two directions of adaptive approaches: MoE-based adaptive fusion, which struggles with uncertainties arising from distinct object configurations, and late fusion for output-level adaptive fusion, which relies on separate detection pipelines and limits comprehensive understanding. In this work, we introduce Cocoon, an *object*- and *feature*-level uncertainty-aware fusion framework. The key innovation lies in uncertainty quantification for heterogeneous representations, enabling fair comparison across modalities through the introduction of a *feature aligner* and a learnable surrogate ground truth, termed *feature impression*. We also propose a training objective to ensure that their relationship provides a valid metric for uncertainty quantification. Cocoon consistently outperforms existing static and adaptive methods across both normal and challenging conditions, derived from natural and artificial corruptions. Furthermore, we demonstrate the validity and efficacy of our uncertainty metric across diverse datasets.

1 INTRODUCTION

In the rapidly evolving field of intelligent systems, accurate and robust 3D object detection is a fundamental and crucial functionality that significantly impacts subsequent decision-making and control modules. With the increasing importance of this field, there has been extensive research on vision-centric (Wang et al., 2022; Liu et al., 2022; 2023a; Wang et al., 2023) and LiDAR-based detection (Yan et al., 2018; Yin et al., 2021; Lang et al., 2019; Zhou et al., 2024), but both approaches have demonstrated weaknesses due to inherent characteristics in sensor data. For example, 2D data lacks geometric information, while 3D data lacks semantic information. To address these limitations, multi-modal approaches that integrate multi-sensory data are actively studied to enhance capabilities in areas such as autonomous vehicles, robotics, and augmented/virtual reality, setting a new standard for state-of-the-art performance in various perception tasks (Chen et al., 2023; Prakash et al., 2021; Bai et al., 2022; Li et al., 2022b; Yan et al., 2023; Li et al., 2022a; 2023; Xie et al., 2023).

The accuracy of multi-modal perception is significantly influenced by the operating context, such as time and the composition of surrounding objects (Yu et al., 2023; Dong et al., 2023). Given the diverse (often complementary) nature of different modalities, maximizing their utility across various objects and contexts remains challenging, particularly for long-tail objects (Feng et al., 2020; Curran et al., 2024). Existing research efforts to address this issue mainly fall into two categories: Mixture of Experts (MoE)-based approaches (Mees et al., 2016; Valada et al., 2017) and late adaptive fusion (Zhang et al., 2023; Lou et al., 2023; Lee & Kwon, 2019). Despite their contributions, existing methods often overlook the varying levels of informativeness among individual objects in the scene by applying weights uniformly across entire features (Fig.1a) or limiting comprehensive understanding/decoding by simply combining outputs from separately trained detectors (Fig.1b), both resulting

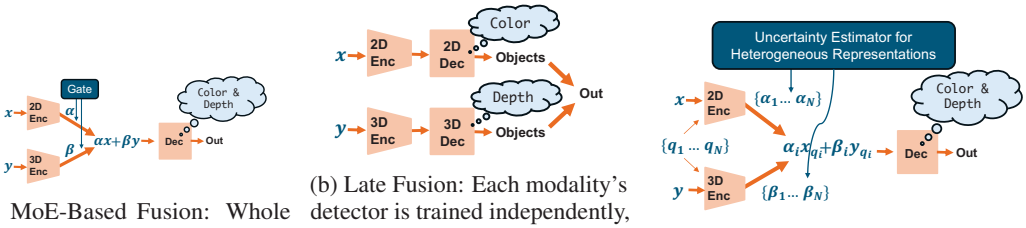

(a) MoE-Based Fusion: Whole feature fusion ignores object-level informativeness variation.

(b) Late Fusion: Each modality's detector is trained independently, limiting accuracy to that of the better-performing modality.

(c) Cocoon (Ours): q_i indicates a query for a potential object.

Figure 1: Existing Fusion Methods[1] and Our Approach.

	Object Distinction	Cross-Modal Feature Enrichment
MoE-Based Fusion (Mees et al., 2016; Valada et al., 2017)	✗	✓
Late Fusion (Lee & Kwon, 2019; Zhang et al., 2023; Lou et al., 2023)	✓	✗
Cocoon (Ours: object- and feature-level uncertainty-aware fusion)	✓	✓

Table 1: Comparison with Prior Works

in sub-optimal performance. To our knowledge, none of these approaches address both object-level uncertainty variation and feature-level (i.e., intermediate) fusion needs, as highlighted in Table 1.

To address these challenges, we introduce Cocoon (Conformity-conscious sensor fusion), which tackles the aforementioned challenges by quantifying uncertainty at both the object and feature levels, and dynamically adjusting the weights of modality-specific features (Fig. 1c). Cocoon comprises four key components: a base object detector, feature alignment, uncertainty quantification, and adaptive fusion. For object-level adaptive fusion, Cocoon uses a query-based architecture as the base object detector, where a fixed number of queries are predetermined, each representing a potential object (Carion et al., 2020a; Chen et al., 2023; Bai et al., 2022). When multi-modal data is received, Cocoon first projects the per-query features, encoded by modality-specific encoders in the base detector, into a common representation space (Jing et al., 2021). Our uncertainty quantification is based on conformal prediction (Angelopoulos & Bates, 2021; Teng et al., 2023) that is widely adopted in practical applications due to its low computational complexity and interpretability (Luo et al., 2022a; Su et al., 2024a; Yang & Pavone, 2023). We propose a new conformal prediction method for heterogeneous representations by introducing the concept of a learnable surrogate ground truth, termed Feature Impression (FI), which enables feature-level uncertainty quantification. While traditional conformal prediction uses detection outputs and their ground truth labels in the output space—which are not available at intermediate stages of the model—our approach bypasses this limitation by employing FI. We demonstrate how FI can guide uncertainty quantification across heterogeneous representations, thus enabling fair comparisons. As such, Cocoon performs linear combination using uncertainty values, achieving object- and feature-level uncertainty-aware fusion.

The main contributions are as follows:

- We observed that ignoring object-level uncertainty in multi-modal object detection leads to suboptimal accuracy, particularly in long-tail conditions such as adverse weather or nighttime, highlighting the need for object-level uncertainty-aware fusion.
- Cocoon achieves object- and feature-level uncertainty-aware fusion by introducing uncertainty quantification for heterogeneous representations. The combination of a feature aligner and feature impression enables efficient and effective measurement of uncertainty at intermediate stages of the model. The resulting weights adjust each modality's contribution, allowing the model to prioritize the modalities with higher certainty to deliver more robust performance.
- In our evaluation on the nuScenes dataset (Caesar et al., 2019), Cocoon demonstrates notable improvement in both accuracy and robustness, consistently outperforming static and other adaptive fusion methods across normal and challenging scenarios, including natural and artificial corruptions. For example, in cases of camera malfunction, Cocoon improves the base model's mAP by 15% compared to static fusion.

Following the review of related work, we present a detailed analysis of the technical challenges in uncertainty-aware fusion within multi-modal perception systems. We then introduce the Cocoon framework and evaluate its effectiveness in addressing these challenges.

[1]While most existing work focuses on 2D perception or the fusion of RGB and depth camera data, we adapt these concepts to our situation.

2 Related Works

Multi-Modal Perception. Multi-modal solutions aim to enhance the accuracy and robustness of perception systems by leveraging diverse data fusion designs, which are typically categorized into early, intermediate, and late fusion. Early fusion combines features at the input level (Malawade et al., 2022b; Putzar et al., 2010; Huang et al., 2020; Sindagi et al., 2019; Vora et al., 2020), while late fusion integrates decisions from independent models at the object level (Sun et al., 2020; Huang et al., 2022; Xiang et al., 2023; Yeong et al., 2021). Favored in recent methods, intermediate fusion enhances accuracy by addressing discrepancies among the inductive biases of different modalities (Chen et al., 2017; Qin et al., 2023; Malawade et al., 2022a). These biases, which vary based on each modality's characteristics, are harmonized via joint learning, ensuring a more cohesive integration of multi-modal data. For example, cameras (Lu et al., 2021; Huang & Huang, 2022; Huang et al., 2021) rely on color and 2D shapes, while LiDAR (Shi et al., 2020; 2019) focuses on reflective properties and 3D shapes. Intermediate fusion combines these biases for a more robust environmental understanding. Techniques have evolved from LiDAR-centric fusion approaches, such as PointPainting and PointAugmenting (Vora et al., 2020; Wang et al., 2021), to more sophisticated architectures like the *Y-shaped* model, which fuses multi-modal features through concatenation, element-wise addition, or an adaptive fusion method (Liu et al., 2023b; Liang et al., 2022; Jiao et al., 2023). Recently, Transformer-based approaches (Chen et al., 2023; Prakash et al., 2021; Bai et al., 2022; Li et al., 2022b; Yan et al., 2023; Li et al., 2022a; 2023; Xie et al., 2023), inspired by DETR (Carion et al., 2020b; Zhu et al., 2020b; Wang et al., 2022), have become popular. They offer efficient detection paradigms using the Hungarian algorithm (Kuhn, 1955) (i.e., the predefined number of queries matched to objects), allowing flexible associations between modalities. Among these, FUTR3D (Chen et al., 2023) and TransFusion (Bai et al., 2022) stand out as the most foundational and representative transformer-based models, significantly influencing the current state-of-the-art in 3D object detection (Prakash et al., 2021; Li et al., 2022b;a; Yan et al., 2023; Li et al., 2023; Xie et al., 2023).

Uncertainty Quantification. Uncertainty quantification in machine learning enhances the trustworthiness and decision-making capabilities of systems by leveraging uncertainties present in both pre-trained models (epistemic uncertainty) and observed data (aleatoric uncertainty). Bayesian techniques are well-known methods in this domain, as they incorporate prior knowledge and update it with new data to estimate posterior distributions for model weights or input data. However, Bayesian methods are computationally intensive, making them less suitable for multi-sensory systems that require timely execution (Blundell et al., 2015; Kendall & Gal, 2017). In such contexts, alternative methods are preferred. One such method is direct modeling, primarily for data uncertainty, which modifies detection models by adding output layers to directly predict output variance (Feng et al., 2021; Su et al., 2024b; 2023). Another approach is Double-M Quantification, which estimates variability for both data and model uncertainty through resampling (Su et al., 2023). Conformal prediction provides prediction intervals using a nonconformity measure and a calibration dataset for addressing both data and model uncertainty (Angelopoulos & Bates, 2021; Teng et al., 2023; Javanmardi et al., 2024). Conformal prediction, with its low computational complexity, distribution-free nature, provability, and interpretability, is most optimal for practical use (Luo et al., 2022a; Su et al., 2024a; Yang & Pavone, 2023).

3 Challenges in Uncertainty-Aware Feature Fusion

Object-Level Uncertainty Variation Phenomenon. Assessing each modality's uncertainty, defined by how reliable its information is about the input scene, is challenging due to the variety of objects within the scene. Additionally, uncertainties are influenced by various factors, including data informativeness and unusualness relative to a pre-trained perception model, making the assessment non-trivial.

We conduct an experiment to empirically demonstrate the impact of diverse uncertainties, as shown in Fig. 2. We apply a baseline perception model (FUTR3D (Chen et al., 2023)), trained to fuse camera and LiDAR data in a 1:1 ratio, to various traffic scenes. We tune the fusion ratio and observe its impact on model effectiveness, measured by the average confidence score. Interestingly, the 1:1 fusion ratio between 2D and 3D data proved to be suboptimal in most scenarios. In daytime scenarios, camera data on distant and small objects is more informative than LiDAR data, suggesting an optimal fusion ratio of 7:3. Conversely, for nearby objects, greater accuracy is achieved when the contribution of LiDAR is increased relative to the camera. Moreover, LiDAR sensors are more effective than cameras at nighttime, indicating that more weight should be assigned to LiDAR inputs to improve perception accuracy.

Overall, this imbalance in the contribution of 2D and 3D data is common and related to various factors such as lighting conditions, object sizes, and distances to the ego agent. These observations

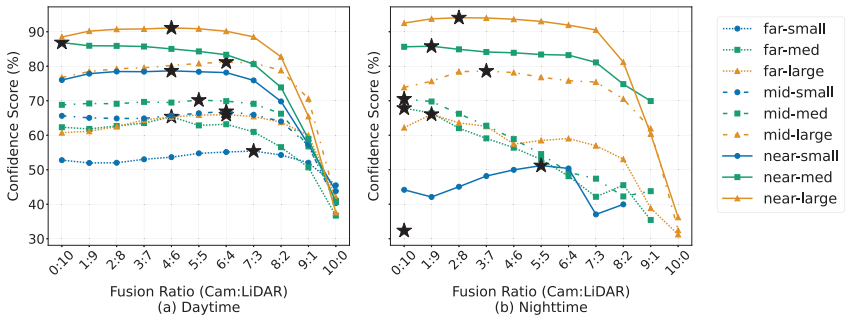

Figure 2: Impact of fusion ratio on average confidence scores under various lighting conditions and object configurations. The black stars denote the optimal camera-to-LiDAR fusion ratios achieving the highest scores for each configuration. Object configurations are categorized based on two attributes: object size and distance to the ego agent. Object sizes are classified into three categories: small (< 2m), medium (2-4m), and large (> 4m). Similarly, distances are segmented into three ranges: near (< 20m), mid-distance (20-40m), and far (> 40m).

highlight the dynamic nature of object-level uncertainties and the need for specific dynamic weighting for each object based on its unique characteristics. To address this, Cocoon quantifies uncertainties for per-object features and dynamically adjusts the weights accordingly.

Undefined Consistent Basis for Comparison. Although existing methods like Cal-DETR (Munir et al., 2023), which computes variance along transformer decoder layers, can quantify uncertainties within a single modality, projecting uncertainties from multi-modal data into a consistent and comparable space remains challenging. This step is crucial for effective multi-modal, uncertainty-aware fusion, where the alignment and comparability of data from different modalities are essential.

The challenge arises from the distinct representation spaces of multi-modal data: 2D data provides color and texture information, whereas 3D data offers depth and geometric insights. We address this challenge through Feature Impression-based feature alignment, motivated by Jing et al. (2021).

4 COCOON

In this section, we introduce Cocoon, an object- and feature-level modality fusion solution. Cocoon employs a query-based architecture with a fixed number of predefined queries, each representing a potential object, enabling it to extract object-level features without relying on final detection outputs (Carion et al., 2020a; Chen et al., 2023; Bai et al., 2022). Specifically, we use FUTR3D (Chen et al., 2023) and TransFusion (Bai et al., 2022)—two foundational and representative query-based models—as our base models. Built on these architectures, Cocoon operates in two phases: an online phase that performs adaptive fusion on test data, and an offline phase that prepares for uncertainty quantification (i.e., conformal prediction) through training and calibration stages.

Fig. 3 illustrates the online mechanism, where we first align per-object features into a common representation space (Sec. 4.2) and then quantify uncertainties for each pair of features (Sec. 4.3). These uncertainties are used as weights (α and β) in the adaptive fusion. For the offline mechanism, we first split the training set into a proper training set and a calibration set. The proper training set is used to train both the base model components and the parameters for uncertainty quantification. Using the calibration set, we create a comparison group containing task-related scores for each calibration sample, which are then used to assess how unusual the online input data is, thereby facilitating uncertainty quantification (Sec. 4.4).

We begin by revisiting the inspiring work, Conformal Prediction (Angelopoulos & Bates, 2021) and Feature CP (Teng et al., 2023), and their limitations in a multi-modal setting. We then explain how we can fairly quantify the uncertainties of multi-modal features on a consistent basis.

4.1 PRELIMINARIES

Conformal Prediction (CP). Conformal prediction, referred to as Basic CP, is an algorithm that outputs a prediction interval, statistically guaranteeing the inclusion of the ground truth (GT) for a given test input (Angelopoulos & Bates, 2021; Teng et al., 2023), rather than merely providing a single prediction value. This prediction interval is established with respect to a significance level (Λ), ensuring that the interval contains the GT with a probability of at least 1-Λ, as follows:

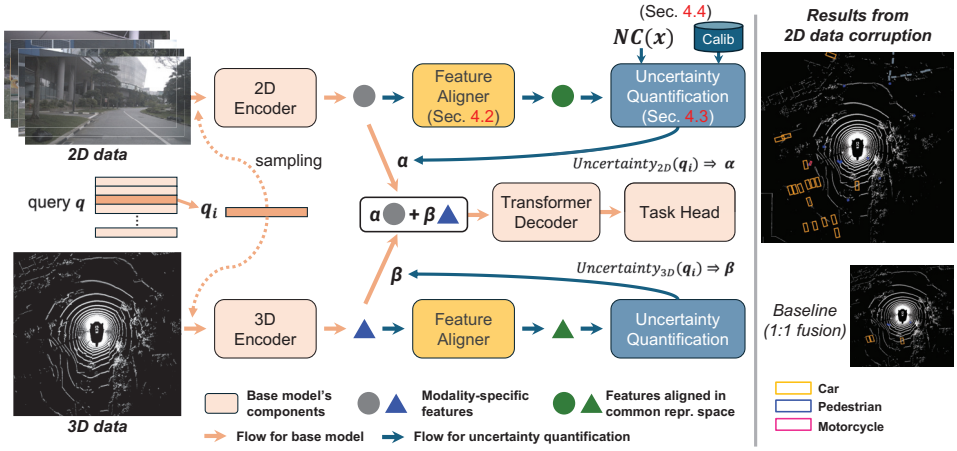

Figure 3: Cocoon Online Procedure (left) and Example Results (right): Cocoon operates on top of base model components. The feature aligner projects per-object features (●, ▲) into a common representation space. Next, uncertainties are estimated for each feature pair (●, ▲) and converted into weights (α and β) for adaptive fusion. These weights amplify/attenuate the contribution of each modality's original feature (●, ▲) to the fused feature, which is then used in the basemodel's decoder.

Table 2: Summary of Main Symbols: Meaning and Purpose

Symbol	Meaning	Purpose	Section
α, β	Key symbols; α represents the weight of one modality (e.g., camera), and β represents the weight of another (e.g., LiDAR).	Uncertainty-based weights (Dynamic)	§4.3, §5.2, Fig. 3, Fig. 6, Fig. 7
δ, ζ, η	Coefficients in the training loss function.	Hyperparameter	§5.1, Eq. 3
Λ	Significance value used to explain the concept of conformal prediction.	Analysis	§4.1, §5.3, Table 4

$$P(y' \in \mathcal{I}_{1-\Lambda}(x')) \geq 1 - \Lambda,$$

where $\mathcal{I}_{1-\Lambda}(x')$ represents the prediction interval for online test input x'.

The process begins with preparing a training set, a calibration set, a pre-trained model, and the establishment of a nonconformity function. During the offline stage, the nonconformity score $NC_i = \text{Distance}(p_i, q_i)$ is computed for each calibration instance, where p_i and q_i denote the predicted output and the GT of instance i, respectively. The pool of scores is used to gauge how unusual online test data is. In the online stage, the algorithm uses $1 - \Lambda$ to compute the tightest prediction interval that includes the GT with at least $1 - \Lambda$ confidence. This is achieved by calculating the $(1 - \Lambda)$-th quantile from the distribution derived from NC_i, for $i \in$ calibration set. Unlike Basic CP, which quantifies output-space uncertainty using GT labels on calibration samples, we address feature-space uncertainty without relying on modality-specific GT labels.

Feature Conformal Prediction (Feature CP). Teng et al. (2023) extends conformal prediction to the feature level using a pre-trained model M, structured into f (encoder) and g (decoder; task head), formulated as $Y = M(X) = (g \circ f)(X)$, with $\circ$ denoting the composition operator. This method measures nonconformity scores directly at the feature level via the encoder f. For nonconformity measure, a surrogate ground truth v^* is identified through an iterative search (see Fig. 4 (a)) to serve as a proxy for the normal GT within a norm-based nonconformity function: $NC_i = \|f(x_i) - v^*_{x_i}\|$. Here, v^* is meticulously calibrated to closely resemble $g^{-1}(y_i)$. However, applying feature conformal prediction directly to our problem poses challenges, primarily because it assumes *homogeneous* representation across target features—an assumption that does not hold in multi-modal settings.

4.2 Feature Impression-Based Feature Aligner

Core Issue: Lack of Modality-Dedicated Decoder. As illustrated in Fig. 4, a dedicated decoder g often does not exist in multi-modal detection models. The absence of g highlights a core issue, as g plays a crucial role in facilitating the bidirectional movement between output space and feature space. To address this issue, *we perform all operations directly at the feature level*, eliminating the conventional move in/out mechanism. Our intuition is that effectively aggregating multi-modal

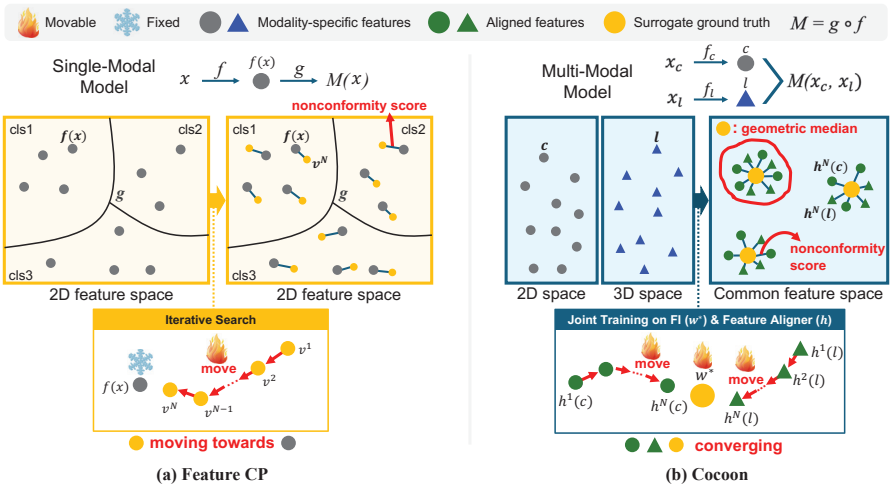

(a) Feature CP (b) Cocoon

Figure 4: Feature CP ***vs.*** Cocoon. In the ***offline*** stage with calibration data, Feature CP identifies the surrogate ground truth (●) for each feature (●) through iterative search. Each ● is derived using the real ground truth label in the output space and the decoder g (serving as a classifier). However, in a multi-modal setting, each feature lacks a modality-specific g. To resolve this, Cocoon leverages joint training of the feature aligner (which projects heterogeneous features (●, ▲) into a common representation space) and the surrogate ground truth (● – termed FI). Our proposed training objective (Eq. 3) ensures that each FI becomes the *geometric median* of aggregated features for valid uncertainty quantification. In the ***offline*** stage, the calibration samples' nonconformity scores (i.e., distance) are collected and used as a comparison target to gauge the uncertainty of online test inputs. In the ***online*** stage with test data, while Feature CP performs iterative search for ●, Cocoon saves time by directly projecting input features through our feature aligner h and using a pre-trained ●.

features into a high-dimensional sphere substantially reduces the need for g. The following sections demonstrate how conformal prediction can operate efficiently with multi-modal features without g.

Based on our intuition, we initiate the process by aligning multi-modal features within a unified representation space using a simple multi-layer perceptron (MLP), inspired by Jing et al. (2021). The key aspect of our approach is the learnable surrogate GT and the joint training of both the surrogate GT and the feature aligner. For clarity, we introduce the new term, feature impressions (FIs; ● in Fig. 4 (b)), with each FI representing a class or a set of similar features and serving as a surrogate GT.

Conditions for FI. As shown in Fig. 4, Feature CP identifies the surrogate GT $v^*_{x_i}$ as the ***nearest*** feature (● in Fig. 4 (a)) to the input sample x_i (●), obtained through iterative search. In the feature space, each x_i has its unique $v^*_{x_i}$, which eventually corresponds to y_i in the output space. In other words, although they measure nonconformity scores in feature space, their final uncertainty values (w.r.t. y_i) are quantified in the output space. Note that if this is a classification task, y_i (e.g., class label) is ***shared*** by multiple x_is belonging to the same class. Based on our intuition, we aim to remove bidirectional movement between feature and output spaces and perform uncertainty quantification directly in the feature space. To achieve this, our surrogate ground truth should satisfy two conditions: (1) we have to identify a ***common*** ground truth for the aligned multi-modal features; (2) given evidence in Feature CP, each FI node (●) should be ***as close as possible*** to the aligned feature (●, ▲) to serve as an effective surrogate GT.

Assuming all distances between an FI node and its corresponding aligned features are ***distinct positive*** values, the FI node should be the ***unique minimizer*** of the sum of all the distances to serve as the effective surrogate GT. This strategic placement establishes the each FI as the ***geometric median***, effectively capturing the essence of the associated features' distribution within the unified representation space. Consequently, we can define our nonconformity function as:

$$NC_i = \|(h \circ f)(x_i) - w^*_{x_i}\|, \tag{1}$$

where h represents the feature aligner, and $w^*_{x_i}$ denotes the x_i's corresponding FI node. This positioning not only enhances efficiency by eliminating the costs associated with g but also simplifies the overall uncertainty quantification process.

4.3 UNCERTAINTY QUANTIFICATION WITH MULTI-MODAL FEATURE SET

Uncertainty quantification entails identifying the most probable FI node at each transformer decoder layer, leveraging insights from the nonconformity function in Eq.1 (see Appendix J for further details).

Finding 1: Feature uncertainty significantly affects the NC score of the top-1 FI node.

Finding 2: Higher feature uncertainty in transformers with multiple decoder layers leads to significant instability in the top-1 FI node across layers.

Based on these observations, our primary uncertainty value is defined using the metric (p-value) employed in conformal prediction (Vovk et al., 2005):

$$\mathcal{P}_{\text{mod}} = \frac{|\{x \in NC_{\text{calib}} : x \geq nc_{\text{mod}}\}|}{|NC_{\text{calib}}|}, \tag{2}$$

where NC_{calib} represents the pool of nonconformity scores computed from all aligned calibration samples, and nc_{mod} denotes the nonconformity score of the current online input data's feature. Leveraging this, the final weight for each modality is calculated as:

$$\mathcal{W}_{\text{mod}} = \frac{\mathcal{Q}_{\text{mod}}\mathcal{S}_{\text{mod}}}{\mathcal{Q}_{\text{mod}}\mathcal{S}_{\text{mod}} + \mathcal{Q}_{\text{other}}\mathcal{S}_{\text{other}}},$$

where $\mathcal{Q}_{\text{mod}} = \frac{\mathcal{P}_{\text{mod}}}{\mathcal{P}_{\text{mod}}+\mathcal{P}_{\text{other}}}$, and $\mathcal{S}_{\text{mod}}$ denotes the stability score, measured by the frequency of top-1 FI changes across decoder layers. *other* refers to the modality opposite to *mod*. The resulting uncertainties are used as weights (α and β in Fig. 3) in adaptive fusion.

4.4 TRAINING AND CALIBRATION STAGES

The training process consists of two stages: the first stage involves training the baseline model using a proper training set, ensuring the pre-trained model has no exposure to the calibration samples. The second stage involves joint training of the feature aligner and FIs, while keeping the base model components frozen. Since the first stage follows the same procedure as the original base model's training (Chen et al., 2023; Bai et al., 2022), we focus on the second stage in this section.

Our nonconformity function (Eq. 1) requires each FI node to act as the *geometric median* for its associated features. A specifically tailored regularizer is crucial to maintain this positioning.

Joint Training of FI and Feature Aligner. The ***Weiszfeld's algorithm*** stands out as a notable solution method for the geometric median problem (Chandrasekaran & Tamir, 1989). For a point y to qualify as the geometric median, it must meet the following criterion:

$$0 = \sum_{i=1}^{m} \frac{x_i - y}{\|x_i - y\|}$$

We can apply this criterion to our problem setting where we have a set of $2N$ features:

$$h_{ci} := h \circ f_c(x_{ci}), i = 1, \ldots, N, \quad h_{li} := h \circ f_l(x_{li}), i = 1, \ldots, N$$

where f_c and f_l are encoders in the model, and x_{ci} and x_{li} represent input data from multiple sensors. With these terms defined, our training objective consists of three terms: $\mathcal{L}_{center}$ for aggregating different modality features around their corresponding FIs (w^*), $\mathcal{L}_{geomed}$ for ensuring that the FIs serve as the geometric median of the aligned features, and $\mathcal{L}_{separate}$ for increasing the distance between the positions of w^*, ensuring clear separation between FIs.

$$\mathcal{L} = \underbrace{\delta \sum_{i=1}^{N} (\|w^* - h_{ci}\| + \|w^* - h_{li}\|)}_{\mathcal{L}_{center}} + \underbrace{\zeta \left\| \sum_{i=1}^{N} \left(\frac{h_{ci} - w^*}{\|h_{ci} - w^*\|} + \frac{h_{li} - w^*}{\|h_{li} - w^*\|} \right) \right\|^2}_{\mathcal{L}_{geomed}} - \underbrace{\eta \sum_{j=1}^{C} \sum_{k=j+1}^{C} \|w_j^* - w_k^*\|^2}_{\mathcal{L}_{separate}} \tag{3}$$

Here, C denotes the number of FI nodes (e.g., the number of classes). This loss function is used to jointly train feature aligner (h) and FIs (w^*). See Appendix C for the derivation of Eq. 3.

Calibration. This process involves computing nonconformity scores (Eq. 1) for each calibration instance using the pre-trained FIs and feature aligner h. The pool of calibration scores is then used to assess how unusual the features of the online input data are, facilitating uncertainty quantification. Further details about the offline process are provided in Appendix H.

Table 3: Accuracy (mAP) Comparison with Baseline Methods Under Different Scenarios. Orange represents original nuScenes validation set, green indicates natural corruptions collected from real-world driving environments, and blue corresponds to artificial corruptions presented in existing work.

Methods	Type	No Corruption	Rainy Day	Clear Night	Rainy Night
Base$_{FUTR3D}$ (Chen et al., 2023)	Static	66.16	68.34	44.51	27.26
AdapNet* (Valada et al., 2017)	MoE-based	62.33	62.82	41.74	21.58
Zhu et al. (2020a)	Self-attention	63.72	64.22	41.17	20.79
Zhang et al. (2023)	Late Fusion	63.93	64.64	42.92	22.56
Cal-DETR (T) (Munir et al., 2023)	Uncertainty-aware	66.24	68.37	44.38	26.29
Cal-DETR (Q) (Munir et al., 2023)	Uncertainty-aware	66.38	68.42	44.61	27.30
Cocoon (Ours)	Uncertainty-aware	**66.80**	**68.89**	**45.68**	**27.98**
Methods	**Type**	**Point Sampling (L)**	**Random Noise (C)**	**Blackout (C)**	**Sensor Misalign.**
Base$_{FUTR3D}$ (Chen et al., 2023)	Static	65.17	60.39	45.13	53.16
AdapNet* (Valada et al., 2017)	MoE-based	61.40	55.83	36.43	46.04
Zhu et al. (2020a)	Self-attention	62.60	56.07	37.82	45.91
Zhang et al. (2023)	Late Fusion	63.24	56.32	39.39	49.61
Cal-DETR (T) (Munir et al., 2023)	Uncertainty-aware	65.29	60.40	44.39	54.87
Cal-DETR (Q) (Munir et al., 2023)	Uncertainty-aware	65.40	60.56	45.25	54.54
Cocoon (Ours)	Uncertainty-aware	**65.89**	**61.83**	**51.87**	**55.61**

Table 4: Accuracy Breakdown w.r.t. Distance.

Corruption	Near (< 20m)		Mid (20-40m)		Far (> 40m)	
	Static	Ours	Static	Ours	Static	Ours
No Corruption	72.3	**72.6**	53.9	**54.3**	7.4	**7.7**
Point Sampling (L)	72.2	**72.5**	53.5	**53.7**	7.0	**7.4**
Random Noise (C)	69.8	**70.9**	49.4	**50.4**	7.4	**7.9**
Blackout (C)	67.0	**69.4**	37.5	**42.8**	3.3	**4.5**
Misalignment	68.4	**69.0**	46.3	**47.1**	4.1	**4.4**

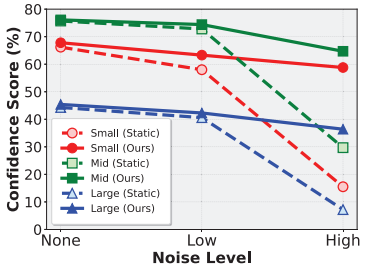

Figure 5: Confidence Score Change.

5 Evaluation

In this section, we evaluate Cocoon's accuracy and robustness across diverse scenarios.

5.1 Evaluation Setup

Dataset. Our evaluations utilize the nuScenes dataset (Caesar et al., 2019), a comprehensive autonomous driving dataset collected from vehicles equipped with a 32-beam LiDAR and 6 RGB cameras. For conformal prediction, we partition the original training dataset into a proper training set and a calibration set with a 6:1 ratio. Details on our dataset are discussed in Appendix A.

Base Models. Cocoon framework is based on 3D object detectors, FUTR3D (Chen et al., 2023) and TransFusion (Bai et al., 2022), known for their unique architectures and influence on recent advancements in the field (Xie et al., 2023; Yan et al., 2023). This section focuses on FUTR3D, with results for TransFusion detailed in Appendix F. FUTR3D encodes 2D and 3D data using ResNet101 He et al. (2016) and VoxelNet Zhou & Tuzel (2018), respectively, fuses the encoded features via concatenation, and then outputs prediction results after passing through six transformer decoder layers. To ensure compatibility with Cocoon, we replace the concatenation with an element-wise sum following the integration of the feature aligner and FI nodes.

Corruption Scenarios. We simulate natural and artificial corruptions that impact online inference results. Natural corruptions include adverse weather and lighting variations, categorized from the nuScenes validation set. For artificial corruptions, 'blackout' simulate camera malfunctions, while other artificial corruptions, identified as challenging conditions (Yu et al., 2023; Dong et al., 2023), represent realistic disturbances. Detailed corruption configurations are provided in Appendix B.

Baselines. AdapNet* (Valada et al., 2017) uses an MoE approach with a trainable gating network; Zhu et al. (2020a) applies self-attention to each modality feature to determine weights; Zhang et al. (2023) employs late fusion with an enhanced Non-Maximum Suppression for output-level adaptive fusion; Cal-DETR (Munir et al., 2023) measures uncertainty using variance in transformer decoder layers. Cal-DETR (T) determines the weights at the tensor level, while Cal-DETR (Q) determines them at the query level, allowing evaluation of object-level adaptive fusion. See Appendix I for details.

Training and Inference Details. For computational resources, 4 A40 GPUs were used for training, and 1 RTX 2080 for calibration and inference. The training process consists of two stages: the first stage involves training the baseline model from scratch using a proper training set, ensuring the pre-trained model has no knowledge of the calibration samples. The second stage involves training the feature aligner and feature impression nodes. We employ an 8-layer MLP for feature

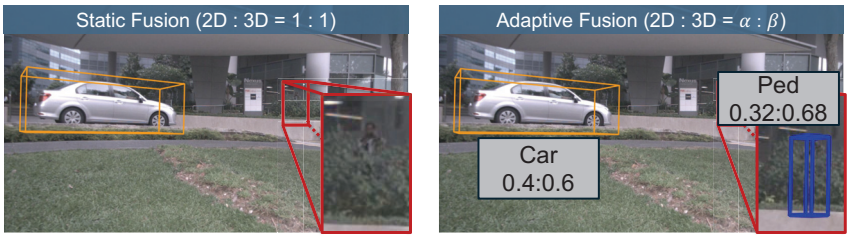

(a) Occluded pedestrian ('Ped.') detected by adaptive fusion.

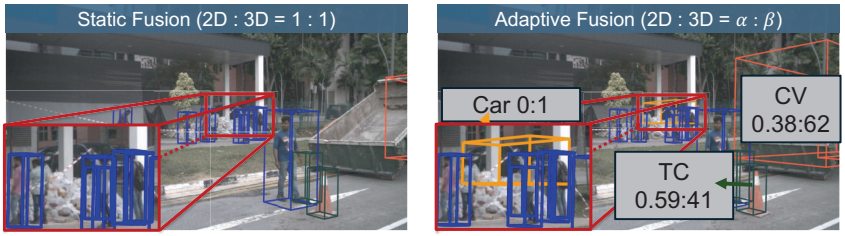

(b) Improved detection on the occluded car (left) and the construction vehicle ('CV'; right). 'TC': traffic cone.

Figure 6: Qualitative Comparison between Static Fusion and Cocoon on Challenging Objects.

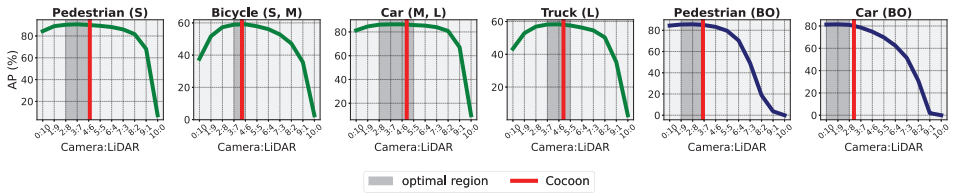

Figure 7: Alignment of Cocoon's resulting weights (α:β, red lines) with optimal regions (grey area). The optimal region is determined as the area within a margin of 0.5 from the peak AP value. "S": small, "M": medium, "L": large, "BO": blackout.

aligner to align modality-specific features to a 128-dimensional representation space. Each FI node indicates per-class feature space within this common representation space. For the first training stage, the baseline models were trained using the same hyperparameters (e.g., learning rate) as those used in original models. In the second stage, a single batch size was used without changing other hyperparameters. Inference was conducted with a single batch size. In Eq. 3, we set $\delta = \frac{5}{\text{num\_queries}}$, $\zeta = \frac{3}{\text{num\_queries}}$, and $\eta = \frac{1}{7 \times \text{num\_queries}}$. See Appendix D for these coefficient values and further details.

5.2 Evaluation on FUTR3D

Quantitative Comparison. Table 3 presents Cocoon's accuracy and robustness across various scenarios. Cocoon consistently outperforms other baselines in both normal and unpredictable environments. For further analysis, we compare the static 1:1 fusion (the original fusion method in the base model) and Cocoon from different perspectives. In Table 4, we break down accuracy based on object locations (distance from the ego agent). Cocoon demonstrates better accuracy in all cases. Notably, the improvements are more significant for mid-distance and far-away objects, which tend to have smaller pixels and sparser points, emphasizing Cocoon's robustness for more challenging objects.

We also evaluate Cocoon's robustness to varying noise levels to assess its generalizability. Fig. 5 presents results under different severities of random noise interference applied to 2D data. "None" represents normal conditions, "Low" introduces uniform noise in the range of -50 to 50, and "High" adds noise in the range of -150 to 150. For fair comparison, we only evaluate commonly detected objects across both static fusion and Cocoon fusion at all noise levels. Even under extreme noise, Cocoon exhibits less perturbation in the confidence scores of objects, demonstrating its ability to mitigate the impact of corrupted modalities and maintain detection accuracy in diverse conditions.

Alignment between Cocoon and Optimal Region. Our primary hypothesis is that optimally weighting different modalities can enhance detection performance, leading to improved APs. To validate this, we assess how well the α and β determined by Cocoon align with the optimal weights. Fig. 7 illustrates this alignment across various object categories in both normal and blackout scenarios. The alignment is consistently observed across diverse object sizes in both conditions, supporting our hypothesis.

Table 5: Comparison of NC Function Effectiveness Across 10 Datasets ($\Lambda = 0.1$). Run 5 times for mean/standard deviation. 'Abs Diff' refers to the absolute difference between the mean and the ideal target of 90%, indicating NC score validity (lower is better). Our method consistently outperforms others, demonstrating the effectiveness of FI, a geometric median-based surrogate ground truth.

Dataset	BasicCP (Angelopoulos & Bates, 2021)	Abs Diff ↓	Feature CP (Teng et al., 2023)	Abs Diff ↓	Ours	Abs Diff ↓
Meps19	90.51 ± 0.25	0.51	90.55 ± 0.21	0.55	90.24 ± 0.65	**0.24**
Meps20	89.80 ± 0.75	0.20	89.76 ± 0.74	0.24	90.02 ± 0.72	**0.02**
Meps21	89.92 ± 0.66	0.08	89.94 ± 0.66	0.06	90.05 ± 0.65	**0.05**
Community	89.82 ± 1.15	**0.18**	89.62 ± 1.01	0.38	90.18 ± 1.30	**0.18**
Facebook1	90.12 ± 0.40	0.12	90.08 ± 0.40	0.08	89.98 ± 0.22	**0.02**
Facebook2	89.95 ± 0.16	0.05	89.96 ± 0.18	0.04	89.98 ± 0.23	**0.02**
Star	90.30 ± 1.42	0.30	90.35 ± 1.21	0.35	90.02 ± 1.73	**0.02**
Blog	90.11 ± 0.3	0.11	90.06 ± 0.39	**0.06**	89.94 ± 0.31	**0.06**
Bio	90.23 ± 0.3	0.23	90.23 ± 0.37	0.23	90.13 ± 0.21	**0.13**
Bike	89.66 ± 1.04	0.34	89.62 ± 0.81	0.38	90.25 ± 1.09	**0.25**

Qualitative Results. As shown in Fig. 6, Cocoon dynamically adjusts the weights between 2D and 3D data, thereby improving detection performance under complex conditions (e.g., occluded objects).

Limitations. The primary limitation is the runtime overhead, as discussed in Appendix K. When using FUTR3D, we observe a 0.5-second increase in latency. To mitigate this, computing nonconformity scores only in the last three decoder layers reduces latency while maintaining better robustness than static fusion. In the section, we also present further methods to minimize this latency gap (e.g., reducing the number of queries). Another limitation is the presence of meaningless queries. Transformer-based architectures, like FUTR3D, often predefine more queries (900) than necessary (up to 200). We found that when α exceeds 0.7, which leads to suboptimal results in all cases in Fig. 2, the meaningless queries predominate, impacting final output due to layer normalization. To address this issue, a clipping strategy is applied, whereby meaningless queries undergo static fusion to ensure stable performance. Fig. 6 shows that queries matched to actual objects remain unaffected by clipping.

5.3 Validity of the Proposed Nonconformity Function

In this section, we aim to quantify uncertainty at the feature level, similar to Feature CP (Teng et al., 2023), but with a different approach. The effectiveness of the nonconformity (NC) function is quantitatively validated through a coverage check, a method widely used in conformal prediction research. Our evaluation examines the alignment between the prediction interval at a given significance level (Λ) and the actual ground truth coverage. For this regression task, our feature aligner projects all features so that they cluster around a single FI node.

Following previous studies, we also use 10 uni-dimensional real-world datasets for validation. Several datsets (bio, bike, community, facebook1, and facebook2) are sourced from the UCI Machine Learning Repository (Kelly et al., 2023; Singh, 2016). Additionally, we utilize data from the Blog Feedback dataset (Buza, 2014), the STAR dataset (Achilles et al., 2008), and the Medical Expenditure Panel Survey datasets (meps19, meps20, and meps21) (Cohen et al., 2009).

In Table 5, our nonconformity function closely aligns with the specified significance level (0.1), consistently including the ground truth in the prediction interval 90% of the time. This demonstrates the effectiveness of our method, leveraging FI (geometric median-based surrogate ground truth), with empirical coverage highlighting the model's proper calibration and effective uncertainty quantification. Qualitative validation on 3D object detection is provided in Appendix **??**.

6 Conclusion & Future Work

In this work, we introduced Cocoon, an uncertainty-aware adaptive fusion framework designed to address the limitations of existing modality fusion methods in 3D object detection. By achieving object- and feature-level uncertainty quantification via conformal prediction, Cocoon enables more effective fusion of heterogeneous representations, enhancing accuracy and robustness across various scenarios.

For future work, we plan to extend Cocoon to accommodate additional types and numbers of modalities, such as fusing camera, LiDAR, and radar for autonomous vehicles and robotics, or combining vision and language for VLMs (Yang et al., 2023; Liu et al., 2024; Team et al., 2023). This broader applicability will enable systems to integrate diverse modalities more effectively, enhancing their ability to interpret complex, challenging environments in ways that mirror human cognition.

ACKNOWLEDGEMENTS

We express our gratitude to our area chairs and anonymous reviewers for their invaluable feedback. This work was supported by NSF under the National AI Institute for Edge Computing Leveraging Next Generation Wireless Networks, Grant 2112562, in addition to grants CMMI-2038215 and CNS-2321532.

REFERENCES

C.M. Achilles, Helen Pate Bain, Fred Bellott, Jayne Boyd-Zaharias, Jeremy Finn, John Folger, John Johnston, and Elizabeth Word. Tennessee's Student Teacher Achievement Ratio (STAR) project, 2008. URL https://doi.org/10.7910/DVN/SIWH9F.

Agency for Healthcare Research and Quality. Data Use Agreement for MEPS. 2017. URL https://meps.ahrq.gov/data_stats/download_data/pufs/h181/h181doc.shtml#Data.

Anastasios N Angelopoulos and Stephen Bates. A gentle introduction to conformal prediction and distribution-free uncertainty quantification. *arXiv preprint arXiv:2107.07511*, 2021.

Xuyang Bai, Zeyu Hu, Xinge Zhu, Qingqiu Huang, Yilun Chen, Hongbo Fu, and Chiew-Lan Tai. Transfusion: Robust lidar-camera fusion for 3d object detection with transformers. In *Proceedings of the IEEE/CVF conference on computer vision and pattern recognition*, pp. 1090–1099, 2022.

Charles Blundell, Julien Cornebise, Koray Kavukcuoglu, and Daan Wierstra. Weight uncertainty in neural network. In *International conference on machine learning*, pp. 1613–1622. PMLR, 2015.

Andrew Burnes. Introducing geforce rtx super graphics cards: Best in class performance, plus ray tracing, 2019. URL https://www.nvidia.com/en-us/geforce/news/geforce-rtx-20-series-super-gpus/.

Krisztian Buza. Feedback prediction for blogs. UCI Machine Learning Repository, 2014. DOI: https://doi.org/10.24432/C58S3F.

Holger Caesar, Varun Bankiti, Alex H. Lang, Sourabh Vora, Venice Erin Liong, Qiang Xu, Anush Krishnan, Yu Pan, Giancarlo Baldan, and Oscar Beijbom. nuscenes: A multimodal dataset for autonomous driving. *arXiv preprint arXiv:1903.11027*, 2019.

Nicolas Carion, Francisco Massa, Gabriel Synnaeve, Nicolas Usunier, Alexander Kirillov, and Sergey Zagoruyko. End-to-end object detection with transformers. In *European conference on computer vision*, pp. 213–229. Springer, 2020a.

Nicolas Carion, Francisco Massa, Gabriel Synnaeve, Nicolas Usunier, Alexander Kirillov, and Sergey Zagoruyko. End-to-end object detection with transformers. In *European conference on computer vision*, pp. 213–229. Springer, 2020b.

Ramaswamy Chandrasekaran and Arie Tamir. Open questions concerning weiszfeld's algorithm for the fermat-weber location problem. *Mathematical Programming*, 44:293–295, 1989.

Xiaozhi Chen, Huimin Ma, Ji Wan, Bo Li, and Tian Xia. Multi-view 3d object detection network for autonomous driving. In *Proceedings of the IEEE conference on Computer Vision and Pattern Recognition*, pp. 1907–1915, 2017.

Xuanyao Chen, Tianyuan Zhang, Yue Wang, Yilun Wang, and Hang Zhao. Futr3d: A unified sensor fusion framework for 3d detection. In *proceedings of the IEEE/CVF conference on computer vision and pattern recognition*, pp. 172–181, 2023.

Minkyoung Cho, Yulong Cao, Zixiang Zhou, and Z Morley Mao. Adopt: Lidar spoofing attack detection based on point-level temporal consistency. *arXiv preprint arXiv:2310.14504*, 2023.

Joel W Cohen, Steven B Cohen, and Jessica S Banthin. The medical expenditure panel survey: a national information resource to support healthcare cost research and inform policy and practice. *Medical care*, 47(7_Supplement_1):S44–S50, 2009.

Noah T Curran, Minkyoung Cho, Ryan Feng, Liangkai Liu, Brian Jay Tang, Pedram MohajerAnsari, Alkim Domeke, Mert D Pesé, and Kang G Shin. Achieving the safety and security of the end-to-end av pipeline. *arXiv preprint arXiv:2409.03899*, 2024.

Yinpeng Dong, Caixin Kang, Jinlai Zhang, Zijian Zhu, Yikai Wang, Xiao Yang, Hang Su, Xingxing Wei, and Jun Zhu. Benchmarking robustness of 3d object detection to common corruptions. In *Proceedings of the IEEE/CVF Conference on Computer Vision and Pattern Recognition*, pp. 1022–1032, 2023.

Di Feng, Christian Haase-Schütz, Lars Rosenbaum, Heinz Hertlein, Claudius Glaeser, Fabian Timm, Werner Wiesbeck, and Klaus Dietmayer. Deep multi-modal object detection and semantic segmentation for autonomous driving: Datasets, methods, and challenges. *IEEE Transactions on Intelligent Transportation Systems*, 22(3):1341–1360, 2020.

Di Feng, Ali Harakeh, Steven L Waslander, and Klaus Dietmayer. A review and comparative study on probabilistic object detection in autonomous driving. *IEEE Transactions on Intelligent Transportation Systems*, 23(8):9961–9980, 2021.

Andreas Geiger, Philip Lenz, and Raquel Urtasun. Are we ready for autonomous driving? the kitti vision benchmark suite. In *2012 IEEE conference on computer vision and pattern recognition*, pp. 3354–3361. IEEE, 2012.

Kaiming He, Xiangyu Zhang, Shaoqing Ren, and Jian Sun. Deep residual learning for image recognition. In *Proceedings of the IEEE conference on computer vision and pattern recognition*, pp. 770–778, 2016.

Junjie Huang and Guan Huang. Bevdet4d: Exploit temporal cues in multi-camera 3d object detection. *arXiv preprint arXiv:2203.17054*, 2022.

Junjie Huang, Guan Huang, Zheng Zhu, Yun Ye, and Dalong Du. Bevdet: High-performance multi-camera 3d object detection in bird-eye-view. *arXiv preprint arXiv:2112.11790*, 2021.

Keli Huang, Botian Shi, Xiang Li, Xin Li, Siyuan Huang, and Yikang Li. Multi-modal sensor fusion for auto driving perception: A survey. *arXiv preprint arXiv:2202.02703*, 2022.

Tengteng Huang, Zhe Liu, Xiwu Chen, and Xiang Bai. Epnet: Enhancing point features with image semantics for 3d object detection. In *Computer Vision–ECCV 2020: 16th European Conference, Glasgow, UK, August 23–28, 2020, Proceedings, Part XV 16*, pp. 35–52. Springer, 2020.

Alireza Javanmardi, David Stutz, and Eyke Hüllermeier. Conformalized credal set predictors. *arXiv preprint arXiv:2402.10723*, 2024.

Yang Jiao, Zequn Jie, Shaoxiang Chen, Jingjing Chen, Lin Ma, and Yu-Gang Jiang. Msmdfusion: Fusing lidar and camera at multiple scales with multi-depth seeds for 3d object detection. In *Proceedings of the IEEE/CVF conference on computer vision and pattern recognition*, pp. 21643–21652, 2023.

Longlong Jing, Elahe Vahdani, Jiaxing Tan, and Yingli Tian. Cross-modal center loss for 3d cross-modal retrieval. In *Proceedings of the IEEE/CVF Conference on Computer Vision and Pattern Recognition*, pp. 3142–3151, 2021.

Markelle Kelly, Rachel Longjohn, and Kolby Nottingham. The uci machine learning repository. *URL https://archive. ics. uci. edu*, 2023.

Alex Kendall and Yarin Gal. What uncertainties do we need in bayesian deep learning for computer vision? *Advances in neural information processing systems*, 30, 2017.

Lingdong Kong, Youquan Liu, Xin Li, Runnan Chen, Wenwei Zhang, Jiawei Ren, Liang Pan, Kai Chen, and Ziwei Liu. Robo3d: Towards robust and reliable 3d perception against corruptions. In *Proceedings of the IEEE/CVF International Conference on Computer Vision*, pp. 19994–20006, 2023.

Harold W Kuhn. The hungarian method for the assignment problem. *Naval research logistics quarterly*, 2(1-2):83–97, 1955.

Alex H Lang, Sourabh Vora, Holger Caesar, Lubing Zhou, Jiong Yang, and Oscar Beijbom. Pointpillars: Fast encoders for object detection from point clouds. In *Proceedings of the IEEE/CVF conference on computer vision and pattern recognition*, pp. 12697–12705, 2019.

Hyungtae Lee and Heesung Kwon. Dbf: Dynamic belief fusion for combining multiple object detectors. *IEEE transactions on pattern analysis and machine intelligence*, 43(5):1499–1514, 2019.

Xin Li, Tao Ma, Yuenan Hou, Botian Shi, Yuchen Yang, Youquan Liu, Xingjiao Wu, Qin Chen, Yikang Li, Yu Qiao, et al. Logonet: Towards accurate 3d object detection with local-to-global cross-modal fusion. In *Proceedings of the IEEE/CVF Conference on Computer Vision and Pattern Recognition*, pp. 17524–17534, 2023.

Xueqian Li, Jhony Kaesemodel Pontes, and Simon Lucey. Neural scene flow prior. *Advances in Neural Information Processing Systems*, 34:7838–7851, 2021.

Yanwei Li, Yilun Chen, Xiaojuan Qi, Zeming Li, Jian Sun, and Jiaya Jia. Unifying voxel-based representation with transformer for 3d object detection. *Advances in Neural Information Processing Systems*, 35:18442–18455, 2022a.

Yingwei Li, Adams Wei Yu, Tianjian Meng, Ben Caine, Jiquan Ngiam, Daiyi Peng, Junyang Shen, Yifeng Lu, Denny Zhou, Quoc V. Le, Alan Yuille, and Mingxing Tan. Deepfusion: Lidar-camera deep fusion for multi-modal 3d object detection. In *Proceedings of the IEEE/CVF Conference on Computer Vision and Pattern Recognition (CVPR)*, pp. 17182–17191, June 2022b.

Tingting Liang, Hongwei Xie, Kaicheng Yu, Zhongyu Xia, Zhiwei Lin, Yongtao Wang, Tao Tang, Bing Wang, and Zhi Tang. Bevfusion: A simple and robust lidar-camera fusion framework. *Advances in Neural Information Processing Systems*, 35:10421–10434, 2022.

Shih-Chieh Lin, Yunqi Zhang, Chang-Hong Hsu, Matt Skach, Md E Haque, Lingjia Tang, and Jason Mars. The architectural implications of autonomous driving: Constraints and acceleration. In *Proceedings of the twenty-third international conference on architectural support for programming languages and operating systems*, pp. 751–766, 2018.

Tsung-Yi Lin, Piotr Dollár, Ross Girshick, Kaiming He, Bharath Hariharan, and Serge Belongie. Feature pyramid networks for object detection. In *Proceedings of the IEEE conference on computer vision and pattern recognition*, pp. 2117–2125, 2017.

Haotian Liu, Chunyuan Li, Qingyang Wu, and Yong Jae Lee. Visual instruction tuning. *Advances in neural information processing systems*, 36, 2024.

Yingfei Liu, Tiancai Wang, Xiangyu Zhang, and Jian Sun. Petr: Position embedding transformation for multi-view 3d object detection. *arXiv preprint arXiv:2203.05625*, 2022.

Yingfei Liu, Junjie Yan, Fan Jia, Shuailin Li, Aqi Gao, Tiancai Wang, and Xiangyu Zhang. Petrv2: A unified framework for 3d perception from multi-camera images. In *Proceedings of the IEEE/CVF International Conference on Computer Vision*, pp. 3262–3272, 2023a.

Zhijian Liu, Haotian Tang, Alexander Amini, Xinyu Yang, Huizi Mao, Daniela L Rus, and Song Han. Bevfusion: Multi-task multi-sensor fusion with unified bird's-eye view representation. In *2023 IEEE international conference on robotics and automation (ICRA)*, pp. 2774–2781. IEEE, 2023b.

Yang Lou, Qun Song, Qian Xu, Rui Tan, and Jianping Wang. Uncertainty-encoded multi-modal fusion for robust object detection in autonomous driving. *arXiv preprint arXiv:2307.16121*, 2023.

Yan Lu, Xinzhu Ma, Lei Yang, Tianzhu Zhang, Yating Liu, Qi Chu, Junjie Yan, and Wanli Ouyang. Geometry uncertainty projection network for monocular 3d object detection. In *Proceedings of the IEEE/CVF International Conference on Computer Vision*, pp. 3111–3121, 2021.

Rachel Luo, Shengjia Zhao, Jonathan Kuck, Boris Ivanovic, Silvio Savarese, Edward Schmerling, and Marco Pavone. Sample-efficient safety assurances using conformal prediction. In *International Workshop on the Algorithmic Foundations of Robotics*, pp. 149–169. Springer, 2022a.

Rachel Luo, Shengjia Zhao, Jonathan Kuck, Boris Ivanovic, Silvio Savarese, Edward Schmerling, and Marco Pavone. Sample-efficient safety assurances using conformal prediction. In *International Workshop on the Algorithmic Foundations of Robotics*, pp. 149–169. Springer, 2022b.

Arnav Vaibhav Malawade, Trier Mortlock, and Mohammad Abdullah Al Faruque. Hydrafusion: Context-aware selective sensor fusion for robust and efficient autonomous vehicle perception. In *2022 ACM/IEEE 13th International Conference on Cyber-Physical Systems (ICCPS)*, pp. 68–79. IEEE, 2022a.

Arnav Vaibhav Malawade, Trier Mortlock, and Mohammad Abdullah Al Faruque. Ecofusion: Energy-aware adaptive sensor fusion for efficient autonomous vehicle perception. In *Proceedings of the 59th ACM/IEEE Design Automation Conference*, pp. 481–486, 2022b.

Oier Mees, Andreas Eitel, and Wolfram Burgard. Choosing smartly: Adaptive multimodal fusion for object detection in changing environments. In *2016 IEEE/RSJ International Conference on Intelligent Robots and Systems (IROS)*, pp. 151–156. IEEE, 2016.

Muhammad Akhtar Munir, Salman Khan, Muhammad Haris Khan, Mohsen Ali, and Fahad Khan. Cal-detr: Calibrated detection transformer. *Neural Information Processing Systems (NeurIPS)*, 2023.

NVIDIA. In-vehicle computing for autonomous vehicles. URL `https://www.nvidia.com/en-us/self-driving-cars/in-vehicle-computing/`.

Aditya Prakash, Kashyap Chitta, and Andreas Geiger. Multi-modal fusion transformer for end-to-end autonomous driving. In *Proceedings of the IEEE/CVF Conference on Computer Vision and Pattern Recognition (CVPR)*, pp. 7077–7087, June 2021.

Lisa Putzar, Kirsten Hötting, and Brigitte Röder. Early visual deprivation affects the development of face recognition and of audio-visual speech perception. *Restorative neurology and neuroscience*, 28(2):251–257, 2010.

Zequn Qin, Jingyu Chen, Chao Chen, Xiaozhi Chen, and Xi Li. Unifusion: Unified multi-view fusion transformer for spatial-temporal representation in bird's-eye-view. In *Proceedings of the IEEE/CVF International Conference on Computer Vision*, pp. 8690–8699, 2023.

Shaoshuai Shi, Xiaogang Wang, and Hongsheng Li. Pointrcnn: 3d object proposal generation and detection from point cloud. In *Proceedings of the IEEE/CVF conference on computer vision and pattern recognition*, pp. 770–779, 2019.

Shaoshuai Shi, Chaoxu Guo, Li Jiang, Zhe Wang, Jianping Shi, Xiaogang Wang, and Hongsheng Li. Pv-rcnn: Point-voxel feature set abstraction for 3d object detection. In *Proceedings of the IEEE/CVF conference on computer vision and pattern recognition*, pp. 10529–10538, 2020.

Vishwanath A Sindagi, Yin Zhou, and Oncel Tuzel. Mvx-net: Multimodal voxelnet for 3d object detection. In *2019 International Conference on Robotics and Automation (ICRA)*, pp. 7276–7282. IEEE, 2019.

Kamaljot Singh. Facebook Comment Volume. UCI Machine Learning Repository, 2016. DOI: https://doi.org/10.24432/C5Q886.

Sanbao Su, Yiming Li, Sihong He, Songyang Han, Chen Feng, Caiwen Ding, and Fei Miao. Uncertainty quantification of collaborative detection for self-driving. In *2023 IEEE International Conference on Robotics and Automation (ICRA)*, pp. 5588–5594. IEEE, 2023.

Sanbao Su, Songyang Han, Yiming Li, Zhili Zhang, Chen Feng, Caiwen Ding, and Fei Miao. Collaborative multi-object tracking with conformal uncertainty propagation. *IEEE Robotics and Automation Letters*, 2024a.

Sanbao Su, Songyang Han, Yiming Li, Zhili Zhang, Chen Feng, Caiwen Ding, and Fei Miao. Collaborative multi-object tracking with conformal uncertainty propagation. *IEEE Robotics and Automation Letters*, 2024b.

Jiachen Sun, Yulong Cao, Qi Alfred Chen, and Z. Morley Mao. Towards robust LiDAR-based perception in autonomous driving: General black-box adversarial sensor attack and countermeasures. In *29th USENIX Security Symposium (USENIX Security 20)*, pp. 877–894. USENIX Association, August 2020. ISBN 978-1-939133-17-5. URL https://www.usenix.org/conference/usenixsecurity20/presentation/sun.

Jiachen Sun, Qingzhao Zhang, Bhavya Kailkhura, Zhiding Yu, Chaowei Xiao, and Z Morley Mao. Benchmarking robustness of 3d point cloud recognition against common corruptions. *arXiv preprint arXiv:2201.12296*, 2022.

Gemini Team, Rohan Anil, Sebastian Borgeaud, Yonghui Wu, Jean-Baptiste Alayrac, Jiahui Yu, Radu Soricut, Johan Schalkwyk, Andrew M Dai, Anja Hauth, et al. Gemini: a family of highly capable multimodal models. *arXiv preprint arXiv:2312.11805*, 2023.

Jiaye Teng, Chuan Wen, Dinghuai Zhang, Yoshua Bengio, Yang Gao, and Yang Yuan. Predictive inference with feature conformal prediction. In *The Eleventh International Conference on Learning Representations*, 2023.

Abhinav Valada, Johan Vertens, Ankit Dhall, and Wolfram Burgard. Adapnet: Adaptive semantic segmentation in adverse environmental conditions. In *2017 IEEE International Conference on Robotics and Automation (ICRA)*, pp. 4644–4651. IEEE, 2017.

Sourabh Vora, Alex H Lang, Bassam Helou, and Oscar Beijbom. Pointpainting: Sequential fusion for 3d object detection. In *Proceedings of the IEEE/CVF conference on computer vision and pattern recognition*, pp. 4604–4612, 2020.

Vladimir Vovk, Alexander Gammerman, and Glenn Shafer. *Algorithmic learning in a random world*, volume 29. Springer, 2005.

Chunwei Wang, Chao Ma, Ming Zhu, and Xiaokang Yang. Pointaugmenting: Cross-modal augmentation for 3d object detection. In *Proceedings of the IEEE/CVF Conference on Computer Vision and Pattern Recognition*, pp. 11794–11803, 2021.

Shihao Wang, Yingfei Liu, Tiancai Wang, Ying Li, and Xiangyu Zhang. Exploring object-centric temporal modeling for efficient multi-view 3d object detection. *arXiv preprint arXiv:2303.11926*, 2023.

Yue Wang, Vitor Campagnolo Guizilini, Tianyuan Zhang, Yilun Wang, Hang Zhao, and Justin Solomon. Detr3d: 3d object detection from multi-view images via 3d-to-2d queries. In *Conference on Robot Learning*, pp. 180–191. PMLR, 2022.

Chao Xiang, Chen Feng, Xiaopo Xie, Botian Shi, Hao Lu, Yisheng Lv, Mingchuan Yang, and Zhendong Niu. Multi-sensor fusion and cooperative perception for autonomous driving: A review. *IEEE Intelligent Transportation Systems Magazine*, 2023.

Yichen Xie, Chenfeng Xu, Marie-Julie Rakotosaona, Patrick Rim, Federico Tombari, Kurt Keutzer, Masayoshi Tomizuka, and Wei Zhan. Sparsefusion: Fusing multi-modal sparse representations for multi-sensor 3d object detection. In *Proceedings of the IEEE/CVF International Conference on Computer Vision*, pp. 17591–17602, 2023.

Junjie Yan, Yingfei Liu, Jianjian Sun, Fan Jia, Shuailin Li, Tiancai Wang, and Xiangyu Zhang. Cross modal transformer via coordinates encoding for 3d object dectection. *arXiv preprint arXiv:2301.01283*, 2023.

Yan Yan, Yuxing Mao, and Bo Li. Second: Sparsely embedded convolutional detection. *Sensors*, 18 (10):3337, 2018.

Heng Yang and Marco Pavone. Object pose estimation with statistical guarantees: Conformal keypoint detection and geometric uncertainty propagation. In *Proceedings of the IEEE/CVF Conference on Computer Vision and Pattern Recognition (CVPR)*, pp. 8947–8958, June 2023.

Hongcheng Yang, Dingkang Liang, Dingyuan Zhang, Zhe Liu, Zhikang Zou, Xingyu Jiang, and Yingying Zhu. Avs-net: Point sampling with adaptive voxel size for 3d scene understanding. *arXiv preprint arXiv:2402.17521*, 2024.

Zhengyuan Yang, Linjie Li, Kevin Lin, Jianfeng Wang, Chung-Ching Lin, Zicheng Liu, and Lijuan Wang. The dawn of lmms: Preliminary explorations with gpt-4v (ision). *arXiv preprint arXiv:2309.17421*, 9(1):1, 2023.

De Jong Yeong, Gustavo Velasco-Hernandez, John Barry, and Joseph Walsh. Sensor and sensor fusion technology in autonomous vehicles: A review. *Sensors*, 21(6):2140, 2021.

Tianwei Yin, Xingyi Zhou, and Philipp Krahenbuhl. Center-based 3d object detection and tracking. In *Proceedings of the IEEE/CVF conference on computer vision and pattern recognition*, pp. 11784–11793, 2021.

Kaicheng Yu, Tang Tao, Hongwei Xie, Zhiwei Lin, Tingting Liang, Bing Wang, Peng Chen, Dayang Hao, Yongtao Wang, and Xiaodan Liang. Benchmarking the robustness of lidar-camera fusion for 3d object detection. In *Proceedings of the IEEE/CVF Conference on Computer Vision and Pattern Recognition*, pp. 3188–3198, 2023.

Xinyu Zhang, Zhiwei Li, Zhenhong Zou, Xin Gao, Yijin Xiong, Dafeng Jin, Jun Li, and Huaping Liu. Informative data selection with uncertainty for multimodal object detection. *IEEE Transactions on Neural Networks and Learning Systems*, 2023.

Yin Zhou and Oncel Tuzel. Voxelnet: End-to-end learning for point cloud based 3d object detection. In *Proceedings of the IEEE conference on computer vision and pattern recognition*, pp. 4490–4499, 2018.

Zixiang Zhou, Dongqiangzi Ye, Weijia Chen, Yufei Xie, Yu Wang, Panqu Wang, and Hassan Foroosh. Lidarformer: A unified transformer-based multi-task network for lidar perception. In *2024 IEEE International Conference on Robotics and Automation (ICRA)*, pp. 14740–14747. IEEE, 2024.

Hu Zhu, Ze Wang, Yu Shi, Yingying Hua, Guoxia Xu, and Lizhen Deng. Multimodal fusion method based on self-attention mechanism. *Wireless Communications and Mobile Computing*, 2020(1): 8843186, 2020a.

Xizhou Zhu, Weijie Su, Lewei Lu, Bin Li, Xiaogang Wang, and Jifeng Dai. Deformable detr: Deformable transformers for end-to-end object detection. *arXiv preprint arXiv:2010.04159*, 2020b.

A Dataset Details

Our evaluations utilize the nuScenes dataset, a comprehensive autonomous driving dataset collected from vehicles equipped with a 32-beam LiDAR and 6 RGB cameras (Caesar et al., 2019). This dataset includes 700 training scenes and 150 validation scenes, each lasting 20 seconds and annotated at a frequency of 2 Hz.

Table 6: Scene Distribution

Dataset	Day	Night	Rate (D/N)
Original	616	84	7.3
Training	528	72	7.3
Calibration	88	12	7.3

In preparation for conformal prediction, we have partitioned the training data into a proper training set and a calibration set, using a 6:1 ratio, as shown in Table 6. The proper training set is used to train the parameters of the base detection model, feature aligner, and FI, while the calibration set is applied during the calibration phase.

One crucial assumption of conformal prediction is *exchangeability*, which states that the distribution of a sequence of instances remains invariant under any permutation of these instances. Since different scenes are distinct enough to be considered exchangeable (Luo et al., 2022b), we generate a dataset of exchangeable calibration samples by sampling a single instance (i.e., frame) at random from each scene belonging to calibration set.

B Configurations for Artificial Corruptions

In this paper, we investigate various artificial corruption scenarios, referencing recent benchmarking studies (Yu et al., 2023; Dong et al., 2023). We explore two types of 2D data corruptions (applied to six images), one type of 3D data corruption, and sensor misalignment scenarios.

For 2D data corruption, camera blackout conditions simulate potential camera malfunctions by converting images into entirely black frames. Additionally, we introduce random noise interference to the six images by adding random noise in the range of -50 to 50 to the original RGB values, where each pixel's value ranges from 0 to 255.

For 3D data corruption, we randomly delete 30% of the points in one frame of LiDAR data. LiDAR density decrease is a common corruption in LiDAR data, shown in various datasets (Dong et al., 2023; Sun et al., 2022; Kong et al., 2023). A 30% density decrease, as shown in Dong et al. (2023), significantly impacts accuracy (dropping by 0.39 to 0.5) in 2D-3D fusion models. This corruption arises from adverse weather, surface reflectivity, and sensor resolution issues Dong et al. (2023); Kong et al. (2023), making it representative of long-tail inputs in public datasets (Geiger et al., 2012; Caesar et al., 2019). Furthermore, due to the large memory usage of LiDAR point clouds, many works use random sampling at higher rates (Li et al., 2021; Yang et al., 2024; Cho et al., 2023), making density decrease a more frequent use case.

Sensor misalignment occurs due to calibration errors, malfunctioning components, or aging sensors, causing spatial or temporal misalignment between sensor data (Dong et al., 2023; Yu et al., 2023). Synchronization issues can arise from external/internal factors, such as spatial misalignment caused by severe vibrations when driving on bumpy roads or temporal misalignment due to clock synchronization module malfunctions. Yu et al., 2023 provides an in-depth investigation into both spatial and temporal alignments. Referencing these works, we add random Gaussian noise to the calibration matrices. In the case of the nuScenes dataset, the calibration matrix, *lidar2cam*, is not normalized, showing a range of (-1463.53, 1516.51) with a mean of -127.18 and a standard deviation of 516.67. Like the point density drop, we introduce 33-34% noise, (-500, 500), which leads to a meaningful accuracy drop.

C Derivation of Training Objective

The challenge of identifying a point that minimizes the sum of unsquared distances to all other points characterizes the geometric median problem. The ***Weiszfeld's algorithm*** stands out as a notable solution method for this problem (Chandrasekaran & Tamir, 1989). For a point y to qualify as the geometric median, it must meet the following criterion:

$$0 = \sum_{i=1}^{m} \frac{x_i - y}{\|x_i - y\|}$$

This formula confirms that y, distinct from all other points, accurately represents the geometric median, underpinning the efficacy of our nonconformity function.

Based on this algorithm, we can apply this to our problem setting where we have a set of $2N$ features:

$$h_{ci} := h \circ f_c(x_{ci}), i = 1, \ldots, N, \quad h_{li} := h \circ f_l(x_{li}), i = 1, \ldots, N$$

where f_c and f_l are encoders in the model, and x_{ci} and x_{li} represent input data from multiple sensors. With these terms defined, the goal is to ensure that w^* is the *geometric median* of this set of features:

$$w^* = \arg\min_{w} \sum_{i=1}^{N} \left(\|w - h_{ci}\| + \|w - h_{li}\| \right). \tag{4}$$

Assuming w^* is distinct from each feature $w^* \neq h_{ci}, w^* \neq h_{li}$, then the sufficient and necessary optimality condition for problem equation 4 is

$$0 = \sum_{i=1}^{N} \left(\frac{h_{ci} - w^*}{\|h_{ci} - w^*\|} + \frac{h_{li} - w^*}{\|h_{li} - w^*\|} \right). \tag{5}$$

Therefore, we can design a loss function to penalize the violation of equation 5

$$\mathcal{L}_{geomed} = \left\| \sum_{i=1}^{N} \left(\frac{h_{ci} - w^*}{\|h_{ci} - w^*\|} + \frac{h_{li} - w^*}{\|h_{li} - w^*\|} \right) \right\|^2. \tag{6}$$

If $\mathcal{L}_{geomed}$ is zero, it confirms that w^* satisfies the geometric median condition as defined in equation 4. As training progresses, the positions of w^* tend to converge, which could potentially cause ambiguities in distinguishing between them. To address this issue, we introduce a penalty, $\mathcal{L}_{separate}$, for increasing distances between the positions of w^*, aiming to maintain clear separations. Consequently, our total loss function incorporates this additional penalty:

$$\mathcal{L} = \delta \underbrace{\sum_{i=1}^{N} (\|w^* - h_{ci}\| + \|w^* - h_{li}\|)}_{\mathcal{L}_{center}} + \zeta \underbrace{\left\| \sum_{i=1}^{N} \left(\frac{h_{ci} - w^*}{\|h_{ci} - w^*\|} + \frac{h_{li} - w^*}{\|h_{li} - w^*\|} \right) \right\|^2}_{\mathcal{L}_{geomed}} - \eta \underbrace{\sum_{j=1}^{C} \sum_{k=j+1}^{C} \|w_j^* - w_k^*\|^2}_{\mathcal{L}_{separate}} \tag{7}$$

where C denotes the number of FI nodes (e.g., the number of classes). The resulting loss function will be used to jointly train feature aligner h and feature impression w^*.

D Training Details

The training process consists of two stages: the first stage involves training the baseline model from scratch using a proper training set, ensuring the pre-trained model has no knowledge of the calibration instances. The second stage involves training the feature aligner and feature impression nodes.

For the first training stage, the baseline models were trained using the same training objective and hyperparameters (e.g., number of epochs, learning rate, etc.) as those used in existing models. In the second training stage, a single batch size was used with the same hyperparameteres as the first stage. Here, we use the proposed training loss function (Eq. 7). We set $\delta = \frac{5}{\text{num\_queries}}$, $\zeta = \frac{3}{\text{num\_queries}}$, and $\eta = \frac{1}{7 \times \text{num\_queries}}$. The coefficient values are determined empirically for stable loss convergence and improved learning of positions. For δ and ζ, we observed that $\mathcal{L}_{center}$ and $\mathcal{L}_{geomed}$ values scale similarly, but $\mathcal{L}_{center}$ converges more slowly. Therefore, we assigned a higher priority to δ than ζ with a ratio of 5:3.

Regarding η, if the contribution of $\mathcal{L}_{separate}$ is small, the distance between w^* of different classes becomes smaller, causing ambiguities in distinguishing between them. Conversely, a large contribution of $\mathcal{L}_{separate}$ disrupts loss convergence and training stability. Through iterative adjustments, we found that $\frac{1}{7 \times \text{num\_queries}}$ yields optimal results. Fig. 8 shows the loss variation with respect to the η value.

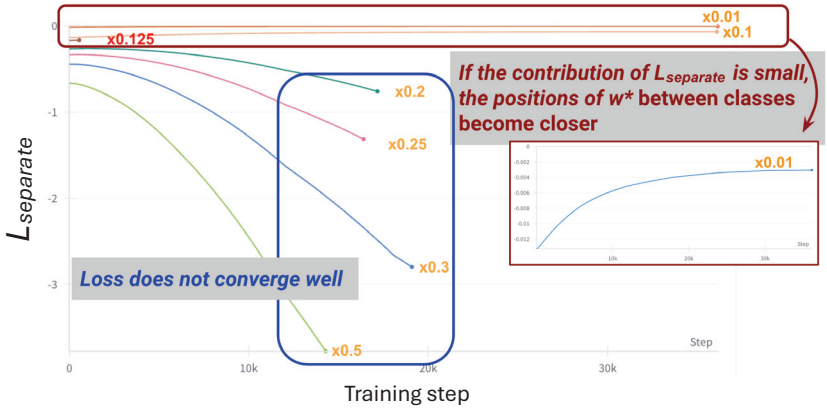

Figure 8: Coefficient Values in Training Objective. This plot shows the effect of the gamma value on $L_{separate}$ with seven separate training progressions. Different curves represent different training settings of gamma values. The text located next to each curve indicates the gamma value for each training ($\frac{1}{num\_queries}$ is omitted). This figure shows how we can choose the gamma value, which ensures both better loss convergence and stable learning of w^*.

E Ablation Study

This section presents an ablation study to assess the contribution of each component. As the feature aligner (FA) and feature impression (FI) are designed for uncertainty quantification based on conformal prediction, we conducted the ablation study hierarchically as follows.

Uncertainty quantification (UQ) vs. Object-level dynamic weighting. Table 7 demonstrates that object-level dynamic weighting is ineffective without UQ, and vice versa, highlighting their mutual dependence. When both are disabled, static fusion is performed through concatenation. Without conformal prediction, a simple MLP model generates a weight value for each object query. When object-level dynamic weighting is disabled, the nonconformity score in UQ is computed for the entire input feature.

Table 7: Performance evaluation of different configurations under various conditions. ✓ indicates the presence of a component.

UQ	Dynamic Weighting	No Corruption	Rainy Day	Clear Night	Rainy Night	Cam. Blackout	Avg. Latency (sec)
		66.16	68.34	44.51	27.26	45.13	0.91 ± 0.02
	✓	63.01	63.51	42.01	21.91	37.01	0.91 ± 0.03
✓		66.2	68.37	44.52	27.3	45.21	1.26 ± 0.04
✓	✓	66.8	68.89	45.68	27.98	51.87	1.27 ± 0.04

Uncertainty Quantification Analysis. We also conduct an ablation study within the scope of uncertainty quantification, examining: 1) The impact of feature aligner (FA) layer count (Table 8), 2) The impact of feature impression (FI) vector dimension (Table 9), 3) The impact of the portion of decoder layers involved in UQ (Table 10). By integrating these findings, we determine the best configuration combination (Table 11). Applying this configuration across all decoder layers reduces the overhead to **0.24 seconds**, while improving accuracy by **0.58%** over static fusion.

Table 8: Performance evaluation with varying FA layer counts.

FA layer count	FI dimension	No Corruption	Rainy Day	Clear Night	Rainy Night	Cam Blackout	Avg. Latency (sec)
2	128	66.01	68.18	44.39	26.99	43.89	1.16 ± 0.05
4	128	66.67	68.56	45.53	27.41	50.99	1.19 ± 0.04
6	128	66.82	68.90	45.55	27.56	51.45	1.24 ± 0.05
8	128	66.80	68.89	45.68	27.98	51.87	1.27 ± 0.04

Table 9: Performance evaluation with varying FI dimensions.

FA layer count	FI dimension	No Corruption	Rainy Day	Clear Night	Rainy Night	Cam Blackout	Avg. Latency (sec)
8	32	66.73	68.91	45.62	27.91	51.81	1.16 ± 0.03
8	64	66.72	68.96	45.64	27.85	51.79	1.21 ± 0.04
8	128	66.80	68.89	45.68	27.98	51.87	1.27 ± 0.04

Table 10: Performance evaluation with varying UQ decoder counts.

UQ Decoder Count	FA Layer Count	FI Dimension	No Corruption	Rainy Day	Clear Night	Rainy Night	Cam Blackout	Avg. Latency (sec)
3	8	128	66.28	68.17	45.11	27.32	51.3	1.13 ± 0.03
6	8	128	66.80	68.89	45.68	27.98	51.87	1.27 ± 0.04

F Evaluation on TransFusion

To demonstrate Cocoon's applicability to other transformer-based detectors, we evaluate it using TransFusion (Bai et al., 2022). TransFusion consists of 2D (ResNet50 He et al. (2016) and FPN Lin et al. (2017)) and 3D (VoxelNet Zhou & Tuzel (2018)) encoders, along with a single transformer decoder layer that uses an *element-wise sum* to combine the 2D and 3D features obtained from the attention mechanisms. See Appendix G for further reconfiguration details.

As shown in Table 12, Cocoon achieves better or comparable accuracy under various corruption scenarios compared to baseline methods. These results use a small set of the nuScenes validation set (120 samples). Since TransFusion has only a single transformer decoder layer, we cannot apply Cal-DETR (T) and Cal-DETR (Q) (Munir et al., 2023), which require multiple decoder layers for uncertainty quantification.

G Base model Reconfiguration Details

FUTR3D. To use FUTR3D as our base model, concatenation (for feature fusion) is replaced with an element-wise sum. This modification maintains accuracy, with both configurations achieving an mAP of 67.39% after training with the proper training set.

TransFusion. TransFusion consists of 2D and 3D encoders, along with a single transformer decoder layer that uses an element-wise sum to combine the features obtained from attention mechanism. Therefore, unlike FUTR3D, TransFusion satisfies our requirement for an element-wise sum.

Currently, due to the need for calibration data separate from the training data, we train the model using only the proper training set. However, obtaining an independent calibration set (100 samples) would allow us to skip the first training stage, requiring only the feature aligner and FIs to be trained with the original nuScenes training set.

H Offline Preparation for Conformal Prediction

During the offline stage of conformal prediction preparation, we first prepare a proper training set and calibration set by splitting the original training set, unless a separately collected dataset is available for calibration. The pivotal process is the calibration step, which computes nonconformity scores (see Eq. 1) for each instance in the calibration set, establishing benchmarks against which new test instances are evaluated.

Model Reconfiguration. Depending on the initial fusion approach used, specific adjustments are made to the model. For instance, models initially using feature concatenation are reconfigured to adopt an element-wise sum, supplemented by a simple multi-layer perceptron (MLP) with one or two fully connected layers, allowing for a linear combination at a 1:1 fusion ratio. This reconfiguration is confirmed to maintain detection accuracy, as exemplified by the FUTR3D model, which retains its original accuracy of 67.3% post-adaptation. Additional details on model reconfiguration are discussed in Appendix G.

Training. This phase involves retraining the model with the designated training set, utilizing the specialized loss function detailed in Sec. 4.4. The focus is on aligning and imprinting features to ensure the model's readiness for conformal prediction.

Table 11: Best configuration combination for uncertainty quantification.

UQ decoder count	FA layer count	FI dimension	No Corruption	Rainy Day	Clear Night	Rainy Night	Cam Blackout	Avg. Latency (sec)
6	4	32	66.59	68.21	45.17	27.08	50.45	1.15 ± 0.03

Table 12: Accuracy (mAP) gain of Cocoon across various corruptions and object categories. 'Ours': the integration of TransFusion and Cocoon. Categories that do not belong to any scene are omitted. Base$_{Trans}$: (Bai et al., 2022), AdapNet*: (Valada et al., 2017)

Corruption Type	Baseline	Car	Truck	Bus	Pedestrian	Bicycle	T.C.	Total
No Corruption	**Base**$_{Trans}$	**88.2**	43.7	93.4	95.4	57.5	65.5	74.0
	AdapNet*	86.7 (-1.5)	**52.4** (+8.7)	**94.3** (+0.9)	94.9 (-0.5)	54.7 (-2.8)	60.4 (-5.1)	73.9 (-0.1)
	Ours	**88.2** (+0)	45.1 (+1.4)	93.6 (+0.2)	**95.6** (+0.2)	**59.3** (+1.8)	**66.6** (+1.1)	**74.7** (+0.7)
Misalignment	**Base**$_{Trans}$	**86.7**	**34.9**	92.4	94.1	**42.5**	61.2	**68.6**
	AdapNet*	85.1 (-1.6)	16.9 (-18.0)	**93.1** (+0.7)	93.3 (-0.8)	40.6 (-1.9)	54.8 (-6.4)	64.0 (-4.6)
	Ours	86.4 (-0.3)	33.4 (-1.5)	92.1 (-0.3)	**94.3** (+0.2)	**42.5** (+0)	**62.1** (+0.9)	68.5 (-0.1)
Blackout (C)	**Base**$_{Trans}$	**84.7**	27.0	**94.7**	93.8	**43.3**	59.6	67.2
	AdapNet*	83.8 (-0.9)	24.5 (-2.5)	92.5 (-2.2)	91.3 (-2.5)	41.1 (-2.2)	54.9 (-4.7)	64.7 (-2.5)
	Ours	84.6 (-0.1)	**30.4** (+3.4)	**94.7** (+0)	**93.9** (+0.1)	40.2 (-3.1)	**59.9** (+0.3)	**67.3** (+0.1)
Sampling (L)	**Base**$_{Trans}$	**86.6**	41.4	91.4	**94.7**	54.0	66.6	72.5
	AdapNet*	84.6 (-2.0)	**50.7** (+9.3)	**91.9** (+0.5)	93.8 (-0.9)	54.1 (+0.1)	61.6 (-5.0)	72.8 (+0.3)
	Ours	**86.6** (+0)	44.3 (+2.9)	91.4 (+0)	**94.7** (+0)	**55.9** (+1.9)	**67.9** (+1.3)	**73.5** (+1.0)

Calibration. This crucial step involves calculating nonconformity scores for all instances in the calibration set. These scores are derived from the nonconformity function: $NC_i = \|(h \circ f)(x_i) - w^*\|$.

Through these methodical subprocesses—model reconfiguration, training, and calibration—our framework thoroughly prepares the model for effective conformal prediction, ensuring it can generate accurate and reliable predictions consistent with the principles of conformal prediction.

I Baseline Adaptive Methods.

Our study investigates various adaptive fusion methods, which serve as baseline approaches in our comparative analysis (see Table. 3). Since none of the existing methods were originally designed for 3D object detection, we adapt their fusion mechanisms to work with FUTR3D and train them using FUTR3D's original hyperparameters. This ensures that all baseline methods, along with Cocoon, share a common base model, allowing us to focus on comparing the effectiveness of the adaptive fusion mechanisms.

AdapNet* **(Valada et al., 2017)** employs a mixture-of-experts (MoE) approach with a trainable gating network to enable adaptive fusion, as illustrated in Fig. 1a. The gating network, placed after the 2D and 3D encoders, determines the feature weights for each modality. This mechanism learns scalar weights for both encoded features and applies the weights to the entire feature space of each modality, producing a fused feature. **Zhu et al. (2020a)** uses self-attention to determine the weights for each encoded feature. In this approach, the encoded features pass through a self-attention module, and a weighted sum is used to produce the fused feature. **Zhang et al. (2023)** employs a late fusion approach that introduces adaptiveness between detection outputs generated from separate detection pipelines. For the detection outputs of both modalities, they perform an informative data selection process using Non-Maximum Suppression (NMS). The decision-level fusion is achieved by combining the box proposals in an enhanced NMS process that incorporates both Intersection over Union (IoU) and confidence scores. In our implementation, we use two versions of the FUTR3D model—one for 2D data only and the other for 3D data only—and apply the NMS process to the box proposals from each modality. **Cal-DETR (Munir et al., 2023)** measures uncertainty in transformer-based perception architectures by calculating variance across the transformer decoder layers. Since this algorithm was originally designed for unimodal perception, we modified FUTR3D's architecture by adding two transformer blocks (two sets of decoder layers): one for 2D data and another for 3D data. These blocks independently assess the uncertainty for each modality. After applying the weighted sum, the adaptively fused input passes through the original transformer decoder to produce the output.

Cal-DETR (T) determines the weights at the tensor level, while **Cal-DETR (Q)** determines them at the query level, enabling us to evaluate the importance of object-level adaptive fusion.

J Insights from Our Nonconformity Measure Analysis

In Sec. 4.3, we present the findings, also shown below, from applying our nonconformity measures to a real-world dataset (Caesar et al., 2019).

Finding 1: Feature uncertainty significantly affects the NC score of the top-1 FI node.

Finding 2: Higher feature uncertainty in transformers with multiple decoder layers leads to significant instability in the top-1 FI node across layers.

These observations were made using the FUTR3D model, which comprises six transformer decoder layers. Finding 1 is also noted with the TransFusion model. However, due to the TransFusion model having only one decoder layer, Finding 2 is not observed. We will elaborate on the findings using Figs. 9 and 10, and Tables 14, 15, and 16.

When measuring the nonconformity scores for multi-modal features, if the object is clearly visible (Fig. 9), the FI nodes corresponding to the two modalities are mostly the same. The nonconformity scores for the top-1 FI node and the second most promising FI node show a significant difference (Table 14). For Object 1, the correct label corresponds to the car class (FI node **0**), and both sensors predict this accurately, facilitating equal fusion between the camera and LiDAR.

However, when the object is unclear (e.g., overlapping or occlusion cases) (Fig. 10), the nonconformity score for the top-1 FI node is very high, with no significant difference from the second most promising FI node (Table 15). For Object 2, the correct label is the construction vehicle class (FI node **2**), but the FI node selection for both modalities does not match this class. Nevertheless, the LiDAR modality predicted a more stable FI node with a lower top-1 nonconformity score, indicating more certain information.

For Object 3 (a person next to a traffic cone and construction vehicle), recognition with LiDAR is challenging. Here, the camera, excelling at color and small object detection, leads to better perception performance, aligning with our nonconformity measure in terms of top-1 FI node consistency and nonconformity scores (Table 16). Object 3's correct label is the pedestrian class (FI node **8**), and the camera predicts this more stably with a lower nonconformity score compared to the LiDAR. Therefore, the camera is deemed more certain in this case.

FI Node #	0	1	2	3	4	5	6	7	8	9
Class	Car	Truck	C.V.	Bus	Trailer	Barrier	M.C.	Bicycle	Ped	T.C.

Table 13: FI Node Clarification. In this experiment, FI nodes are designed to indicate classes. 'C.V.': Construction Vehicle, 'M.C.': Motorcycle, 'T.C.': Traffic Cone.

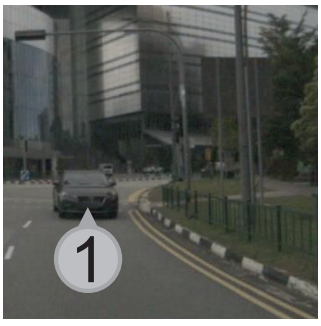

Figure 9: Clearly Visible Car.

Figure 10: Challenging Case.

(a) Top-3 NC Scores Sorted in Ascending Order

Object 2	Camera NC Scores			LiDAR NC Scores		
Layer	1	2	3	1	2	3
0	0.08	9.08	9.75	0.09	9.24	9.88
1	0.07	10.14	11.06	0.09	10.23	11.17
2	0.06	10.65	12.22	0.06	10.74	12.31
3	0.06	11.00	11.24	0.07	11.11	11.35
4	0.06	12.66	12.81	0.08	12.75	12.90
5	0.07	13.56	13.70	0.07	13.66	13.80

(b) Corresponding FI Nodes For Top-3 NC Scores

Object 2	Camera FI Nodes			LiDAR FI Nodes		
Layer	1	2	3	1	2	3
0	0	4	1	0	4	1
1	0	2	1	0	2	1
2	0	1	2	0	1	2
3	0	1	9	0	1	9
4	0	5	8	0	5	8
5	0	1	2	0	1	2

Table 14: NC Score Analysis for Object 1. Correct class in blue.

(a) Top-3 NC Scores Sorted in Ascending Order

Object 2	Camera NC Scores			LiDAR NC Scores		
Layer	1	2	3	1	2	3
0	1.31	8.26	9.11	3.82	6.05	6.73
1	3.91	10.74	11.68	2.40	6.25	7.49
2	7.09	21.22	21.41	4.79	5.98	6.00
3	0.21	6.92	8.69	0.34	6.79	8.60
4	2.16	18.21	18.98	0.20	12.94	13.00
5	6.26	10.44	12.26	4.61	7.90	10.16

(b) Corresponding FI Nodes For Top-3 NC Scores

Object 2	Camera FI Nodes			LiDAR FI Nodes		
Layer	1	2	3	1	2	3
0	8	9	4	4	9	1
1	2	0	4	4	9	1
2	3	2	1	1	2	4
3	1	4	2	1	4	2
4	3	1	9	1	9	0
5	1	3	4	4	2	1

Table 15: NC Score Analysis for Object 2. Correct class in blue.

(a) Top-3 NC Scores Sorted in Ascending Order

Object 3	Camera NC Scores			LiDAR NC Scores		
Layer	1	2	3	1	2	3
0	0.07	9.28	10.28	0.24	9.50	10.54
1	0.12	12.57	12.60	5.19	11.61	13.22
2	0.10	11.31	12.11	0.22	11.57	12.36
3	0.09	10.75	12.72	0.16	10.98	12.92
4	0.07	12.56	12.80	8.71	10.23	12.44
5	0.08	12.23	12.59	0.33	13.02	13.20

(b) Corresponding FI Nodes For Top-3 NC Scores

Object 3	Camera FI Nodes			LiDAR FI Nodes		
Layer	1	2	3	1	2	3
0	8	9	4	8	9	4
1	8	0	9	6	0	8
2	8	4	9	8	4	9
3	8	4	9	8	4	9
4	8	9	0	8	6	0
5	8	4	1	9	1	8

Table 16: NC Score Analysis for Object 3. Correct class in blue.

K Runtime Overhead

	Static: Base model	Adaptive: Base model + Cocoon
FUTR3D	0.91 ± 0.02	1.27 ± 0.04
TransFusion	0.7 ± 0.1	0.7 ± 0.1

Table 17: Comparison of inference latency (in seconds) between static and adaptive fusion. Run 120 times for mean and standard deviation.

Table 17 shows the runtime overhead when Cocoon is integrated. In TransFusion, which uses a single transformer decoder layer processing 200 queries, there is no significant increase in latency compared to static fusion. However, in FUTR3D, which has six transformer decoder layers processing 900 queries, the average latency increases by 0.5 seconds, mainly due to computing nonconformity scores in all six layers. To minimize this latency increase, we performed nonconformity computation only on the last three layers. In this case, the latency can be reduced to 1.3 ± 0.1 seconds, achieving 66.28% accuracy in normal (no corruption) condition and 51.3% accuracy in 2D data corruption (blackout) condition. To further reduce the latency gap between static fusion and Cocoon's adaptive fusion, we can use 200 queries instead of 900, as in TransFusion, or apply model compression (e.g., quantization and pruning) to the feature aligners.

L Fine-Tuning-Based Computational Overhead Mitigation

From the ablation study E, we found that adjusting the MLP layer count and the vector dimension of Feature Impression (FI) can reduce the overhead of 120 ms while maintaining higher accuracy than static fusion.

To further reduce the overhead, we devised a fine-tuning approach: dynamic fusion is applied only to the last decoder layer, and we fine-tune only the components in the later stages of the fusion process (the earlier parts must remain unchanged to preserve the validity of nonconformity score).

Using this fine-tuning approach, we reduced Cocoon's additional overhead (excluding the base model) to 50 ms—a significant reduction of 86% from the previous overhead of 360 ms—while achieving the final accuracy shown in Table 18 on an NVIDIA GeForce RTX 2080 (11 TOPS; Burnes (2019)). Given the computational capability of current AV systems —the most common field where Cocoon can be applied (254 TOPS; NVIDIA)—this overhead is negligible, with total latency within the 100 ms threshold for real-time guarantees (Lin et al., 2018).

Table 18: Performance comparison under different conditions.

Fusion	No Corruption	Rainy Day	Clear Night	Rainy Night	Point Sampling (L)	Random Noise (C)	Avg. Latency (sec)
Static	66.16	68.34	44.51	27.26	65.17	60.39	0.91 ± 0.02
Cocoon (original)	66.80	68.89	45.68	27.98	65.89	61.83	1.27 ± 0.04
Cocoon (fine-tuning)	67.13	69.12	45.70	28.07	66.02	61.99	0.96 ± 0.03

M HANDLING LARGE QUALITY DIFFERENCES ACROSS MODALITIES

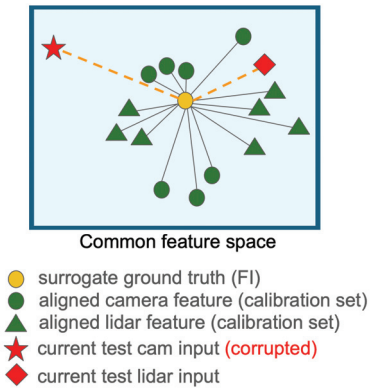

Figure 11: Feature Alignment Outcomes

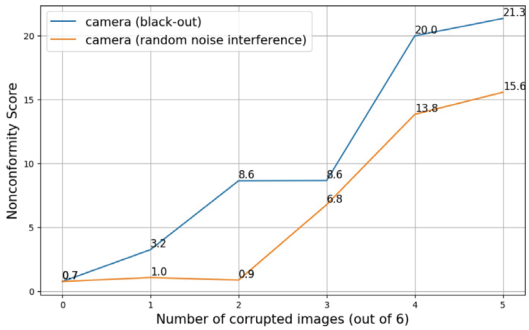

Figure 12: Nonconformity Scores Under Varying Camera Corruption Levels

Figs. 11 and 12 show the feature alignment outcomes and nonconformity scores under conditions of large quality differences across modalities. In this scenario, low-quality data points are positioned farther from the learned surrogate ground truth (i.e., Feature Impression), resulting in lower assigned weights.

N LICENSE OF ASSETS

Code. FUTR3D[2] and TransFusion[3] are both under the Apache-2.0 license.

Datasets. we utilize the nuScenes dataset (Caesar et al., 2019), which is licensed under CC BY-NC-SA 4.0. Appendix 5.3 shows ten different datasets. Several of these datasets, including Bio, Bike, Community, Facebook1, and Facebook2, are sourced from the UCI Machine Learning Repository (Kelly et al., 2023; Singh, 2016), which is licensed under CC BY 4.0. The Blog dataset (Buza, 2014) is also licensed under CC BY 4.0, while the Star dataset (Achilles et al., 2008) is under the CC0 1.0 license. For the Medical Expenditure Panel Survey datasets (Meps19, Meps20, and Meps21) (Cohen et al., 2009), we have the necessary permissions for their use, as we utilize these datasets exclusively for statistical reporting and analysis (Agency for Healthcare Research and Quality, 2017).

[2]https://github.com/Tsinghua-MARS-Lab/futr3d
[3]https://github.com/XuyangBai/TransFusion